ORIGINAL RESEARCH

Evidence of novel crystal structure in cesium-doped sodium zirconate perovskite and its impact in optical and CO_2 sorption properties

**A. Nathan-Abutu · D. Lardizabal-Gutierrez ·
A. Reyes-Rojas**

Abstract The synthesis and crystallographic stability of Cs^+-doped Na_2ZrO_3 perovskite were explored to enhance optical properties and CO_2 sorption at low temperatures (500 °C). Perovskite nanoparticles (~ 20 nm) crystallize in monoclinic C 2/c symmetry and undergo a partial transformation to a new rhombohedral (Hex) $R\bar{3}m$ symmetry during synthesis. The newly obtained atomic coordinates are discussed with respect to their Wyckoff site multiplicity. The incorporation of Cs^+ significantly improves perovskite stability (from $t = 0.807$ to $t = 0.916$). Optical band gap analysis reveals a reduction in photon energy from 3.91 to 3.54 eV, making it a promising photonic material due to its low phonon energy ($\geq 430 cm^{-1}$). Additionally, Cs concentration induces a porous structure that enhances CO_2 capture capacity, as observed in CO_2 sorption analysis.

Introduction

The environmental and energy challenges the world faces over these decades are found to be huge with remarkably few available strategies of solution. These challenges have led to the growing market demands on modern photonic metal and metal oxide perovskites, silica-based, carbon-based materials, and polymer-based nanomaterials, with the capability for miniaturization, higher efficiency, optical and electrical tunable controllable properties, pollution removal capacity, and stable performance [1]. The scientific and engineering communities have taken a remarkable and commendable approach to mitigating these challenges through the design, development, and application of novel nanomaterials. Perovskites, among a wide variety of materials, showed great interest due to their unique optoelectronic (e.g., photochromic, electrochromic) properties that can be processed at low temperatures; photocatalytic as well as CO_2 capture properties, etc. [2]. In the field of material science and technology, nanomaterials play an important and indispensable role in solving/saving

Highlights
- Nonradiative multiphonon relaxation of excited activator ions.
- Nanomaterials are an important integral in solving.
- Increase of sorption and regeneration conversion.
- Optical absorbance spectra of the as-synthesized.
- Nitrogen physisorption analysis for specific surface area.

A. Nathan-Abutu · D. Lardizabal-Gutierrez ·
A. Reyes-Rojas (✉)
Materials Science Department, Centro de Investigación en Materiales Avanzados, Complejo Industrial Chihuahua, Miguel de Cervantes 120, 31109 Chihuahua, S.C.CHIH, Mexico
e-mail: armando.reyes@cimav.edu.mx

A. Nathan-Abutu
Department of Physics, Federal University of Agriculture, Benue State, P.M.B. 2373, Makurdi, Nigeria

major global energy problems faced by all mankind through the development of new and clean energy.

The catalytic properties of perovskite-type oxide allow its application in phosphors [3, 4], biodiesel synthesis [5, 6], and carbon monoxide oxidation [7–9]. Phosphors absorb energy and then emit it as visible light through a process called photoluminescence. The sequestration process of CO_2 involves absorption, adsorption, cryogenic distillation, and membrane separation techniques [10]. The scientific literature has examined the effectiveness of ceramic acceptors, specifically those containing alkaline and earth-alkaline oxides and hydroxides such as Li_2O, LiOH, NaOH, BaO, MgO, and CaO, as promising options for capturing CO_2 from the atmosphere due to their favorable kinetic and thermodynamic properties; however, certain ceramics like CaO exhibit diminished performance over repeated cycles due to sintering deactivation [11–18].

Zirconate materials are renowned for their distinctive characteristics, which encompass a high melting point, exceptional resistance to heat, robust chemical and thermal stability, and the presence of a low phonon energy and a broad optical band gap [4]. Limited research studies have explored the utilization of Li_2ZrO_3 [19–21], Na_2ZrO_3 [11, 22–24] and Li:Na_2ZrO_3 [25] in repeated carbonation-calcination processes, covering a wide temperature range from room temperature to 700 °C.

Since the advent of the Industrial Revolution, there has been a notable acceleration in atmospheric warming, which corresponds to the increased levels of carbon dioxide in the atmosphere. Human ecosystems heavily depend on plants that perform photosynthesis to utilize carbon dioxide for their survival. These plants and forests play a crucial role in continually removing and storing more carbon dioxide from the atmosphere. In natural quantities, carbon dioxide is not problematic, as it is an integral part of the global ecosystem of greenhouse gases responsible for the greenhouse effect. However, the excessive release of carbon dioxide into the atmosphere by human activities like deforestation and industrial processes, which rely on carbon resources such as oil, has led to significant global ecological challenges. Hence, twenty-first-century environmental and energy research has prioritized the development of methods for extracting substantial carbon dioxide from the atmosphere and transforming it into useful, beneficial products

[26–29]. Projected for 2030, annual primary energy production from coal, a fossil fuel source, is expected to reach 3976 million tonnes of oil equivalent (Mtoe), resulting in CO_2 emissions of approximately 38,749 million metric tonnes (MtCO$_2$), with coal contributing to 75% of these emissions [28].

Advanced nano-CO2 harvesting technologies extract carbon dioxide from the atmosphere, converting it into versatile industrial products like methanol, which can be utilized as fuel, solvent, antifreeze, and ethanol diluent [30–33]. The considerable surface-area-to-volume ratio of nanoparticles, coupled with their inherent properties, makes them a highly promising strategy for effectively interacting with CO_2 and facilitating its conversion into valuable products, presenting a potential solution when appropriately employed in the fight against climate change and the reduction of pollution.

The efficiency of Na_2ZrO_3 for CO_2 capture to a greater extent is related to the mobility of Na^+ in $(ZrO_3)_2$ chains because Na^+ ions are located between the $(ZrO_3)_2$ layers; therefore, the diffusion of Na^+ is determined by its structure and morphology [7, 34]. Na_2ZrO_3 having been proven to be a good CO_2 material absorbent, we believe that incorporation of Cs^+ ion into this host matrix will present a synergetic effect that will enhance more CO_2 capturing, our hypothesis is based on the next chemical reaction:

$$Na_{2-x}Cs_xZrO_3 + CO_2 \rightarrow \left(Na_{2-x}Cs_x\right)CO_3 + ZrO_2$$
$$(1)$$
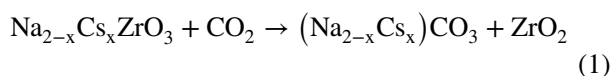
This implies $\left(Cs_xNa_{2-x}\right)CO_3$ will be a mixed compound material of Cs_2CO_3 and Na_2CO_3.

Our research efforts were directed towards synthesizing nanocrystals of $Na_{2-x}ZrO_3$:Cs^+ (with a range of x values from 0 to 0.1) and investigating their crystal structure, optical characteristics, and potential photocatalytic mechanisms related to CO_2 capture. To achieve this, we opted for the citrate-ethylene glycol synthesis route, which allowed for a uniform distribution of Na, Cs, and Zr elements while also leading to smaller crystal sizes and controlled crystal phases, in contrast to the conventional solid-state reaction method [9, 24, 32]. Solid nanomaterial CO_2 sorbent has more capacity for CO_2 capture with better stability of regeneration process than other CO_2 sorption techniques, which require higher energy and more wastage of the sorbent; the sorbent should work at a higher temperature zone above 400 °C for

simultaneous sorption and regeneration activities [34–36]. Zhao et al. [8] reported that nano-Na_2ZrO_3 prepared using a soft chemical route achieved a CO_2 adsorption capacity of 17 wt% at 848 K, 0.5 bar. In 2016, Jo et al. [11] obtained a CO_2 sorption capacity of 17.5–21.0 wt% at 823 K with 1 bar through citrate sol–gel technique of preparation of Na_2ZrO_3 as compared to that obtained by solid-state reaction with CO_2 sorption capacity of 15.8 wt% in 1 bar.

The CO_2 adsorption/desorption cycle process involves the adsorption of carbon dioxide molecules onto solid adsorbent materials, usually with a high surface area, such as metal–organic frameworks (MOFs) or activated carbon or $Na_{2-x}ZrO_3:Cs^+$ adsorbents. During sorption, CO_2 molecules adhere to the sorbent's surface through weak chemical bonds or physical interactions, effectively trapping them in the material's pores.

All prior research concerning the introduction of basic dopants into Na_2ZrO_3 adsorbents has indicated that the CO_2 adsorption performance is influenced by both the choice of dopant and its concentration. Nevertheless, as far as our knowledge extends, the incorporation of Cs into the sodium sites of Na_2ZrO_3 inorganic perovskites has not been explored. In this investigation, we synthesized two sets of Cs-doped Na_2ZrO_3 nanomaterials using the citrate-glycol sol–gel method, followed by annealing at 900 °C to examine their impact on the optical, structural, and CO_2 chemisorption properties of the Na_2ZrO_3 perovskite. These inorganic perovskite-type oxides, exemplified by the novel $Na_{2-x}Cs_xZrO_3$ nanomaterial, hold great potential as intriguing nanomaterials with diverse applications in fields like photonics, fuel cells, catalysis, and electrochemical sensing.

Experimental section

Synthesis of $Na_{2-x}ZrO_3:Cs^+$ perovskite nanomaterials

The raw materials used for the synthesis of $Cs_xNa_{2-x}ZrO_3$ $(0 < x < 0.1)$ nanoparticles are sodium nitrate ($NaNO_3$), cesium nitrate ($CsNO_3$), zirconium (IV) oxynitrate hydrate ($ZrO(NO_3)_2 \cdot xH_2O$), citric acid ($C_6H_8O_7$), ethylene glycol ($C_2H_6O_2$), and ammonium hydroxide (NH_4OH). All chemicals are of analytical grade and used without any further purification. The stoichiometric molar ratios of the starting materials

were $NaNO_3$: $CsNO_3$: $ZrO(NO_3)_2 \cdot xH_2O$: $C_6H_8O_7$: $C_2H_6O_2 = (2-x):x:1:2:1$ $(0 < x < 0.1)$. All precursors, excluding ammonium hydroxide, were dissolved in 60 mL of deionized water and heated at 70 °C for 3 h in a stirred bath. Ammonium hydroxide was then added dropwise until reaching a pH of 5, with continuous stirring for an additional hour. The solution was heated to 80 °C and left exposed to air until a gel formed. This gel was dried overnight at 90 °C in an oven. Subsequently, the resulting powder was ground in an agate mortar and calcined at 900 °C in the air for 4 h. Finally, the samples were naturally cooled to room temperature and finely ground to obtain white powders containing cesium-doped Na2ZrO3 for further research characterization.

Characterization

The phase formation of all the prepared samples was confirmed by XRD-recorded PANalytical X'Pert Pro performed using Cu-K α radiation ($\lambda = 0.1509$ nm) at an X-ray source operated at 40 kV and 30 mA; thermogravimetric analysis (TGA, System-Pyris-1 Perkin Elmer). The Raman spectra were taken at room temperature using a HORIBA Scientific instrument. The IR spectra were conducted using a Thermo Nicolet 6700 device. Optical absorption spectra were acquired using a Thermo Scientific Evolution 220 UV–visible spectrophotometer. Morphology analysis was conducted using a scanning electron microscope (SEM) equipped with an energy-dispersive spectrometer (EDS) attachment, specifically the Hitachi SU3500 SEM. To determine the pore size and volume of the samples, surface area analyses were performed employing Brunauer–Emmett–Teller (BET) theory and Barrett-Joyner-Halenda (BJH) desorption analysis.

Potential CO_2 sorption/regeneration capacity test

The assessment of CO_2 capture performance was conducted using a TGA 500 V20.13 model thermogravimetric analyzer (TGA). After annealing, the resulting powders were introduced into the TGA with sample sizes as indicated in Table 1. Experimental evaluation in the TGA was carried out under the following conditions: 500 °C temperature, an 80% mole fraction of CO_2 in an Ar atmosphere, and a gas flow rate of 150 standard cubic centimeters

Table 1 TGA sorption/regeneration conditions employed during the experimental evaluation

| Sample	% mol. Cs	Compound	Used mass (mg)	Sorption temperature (°C)	Regeneration temperature (°C)	Sorption gas conc., 80% vol	Regeneration gas	Gas flow rate sccm
$X=0$	0	Na_2ZrO_3	14.8340	500	700	CO_2/Ar	Air	100
$X=0.05$	5	$Na_{1.95}Cs_{0.05}ZrO_3$	6.4180	500	700	CO_2/Ar	Air	100
$X=0.1$	10	$Na_{1.9}Cs_{0.1}ZrO_3$	9.3770	500	700	CO_2/Ar	Air	100

per minute (sccm). Regeneration was performed at 700 °C, using air, and a gas flow rate of 100 sccm. Sorption conversion readings were taken when the weight variations in the TGA reached a stable state, while regeneration conversion data was collected after a 15-min interval when the kinetic difference became more apparent. Additionally, the BET surface area, porosity, and pore size were determined through N_2 adsorption using Quantachrome Instruments version 11.03. Prior to these measurements, all samples underwent a 24-h outgassing process in a vacuum at 200 °C to ensure the complete removal of pre-absorbed substances.

Results and discussion

Crystal structure of $Na_{2-x}ZrO_3$:Cs^+ perovskite

The XRD patterns of the powders of $Na_{2-x}ZrO_3$:Cs^+ are presented in Fig. 1. The recorded XRD patterns show sharp and distinct peaks corresponding to 2θ and reflection plans at 16.164° (200), 18.415° (011), 32.659° (400), 33.643° (131), 38.736° ($\bar{3}$ 31), 50.561° ($\bar{5}$ 31), 55.342° (531), 56.616° (060), and 59.274° (260). The host matrix Na_2ZrO_3 can present two defined phases: either monoclinic (ICDD 035–0770) or hexagonal (ICDD 21–1179)

Fig. 1 Rietveld refinement of the XRD patterns; bottom inset shows the simple rhombohedral (Hex) structure of $Na_{2-x}ZrO_3$:Cs^+ nanocrystals projected along [110] direction
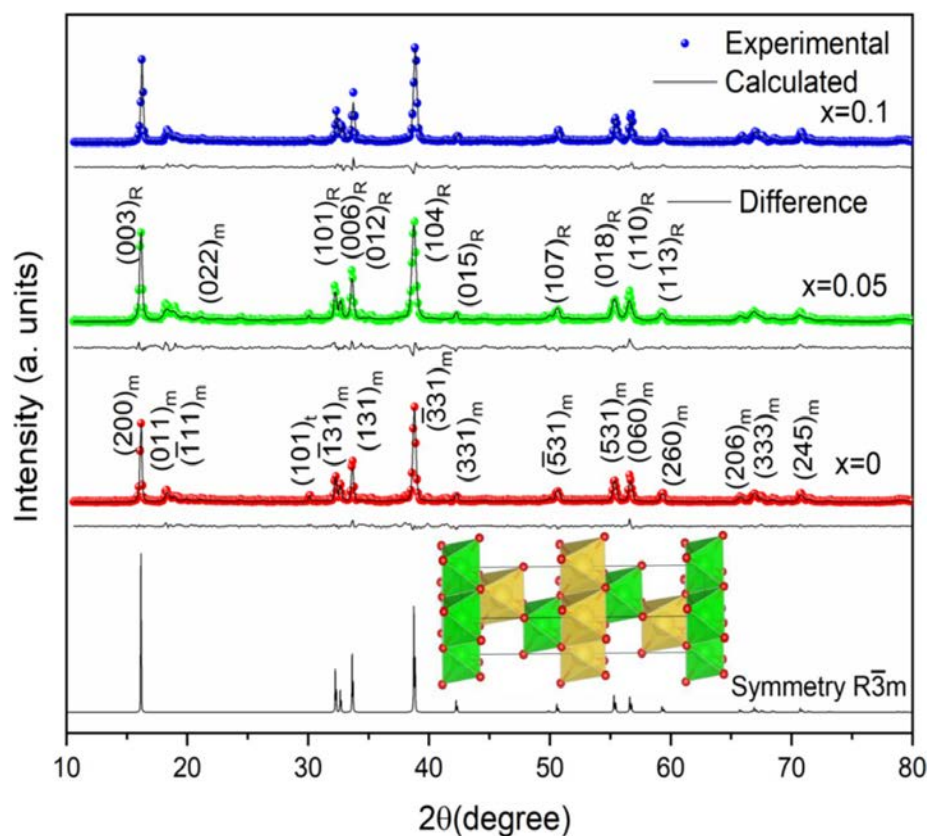
phases [35]. The complete crystallographic patterns recorded for all the samples confirm that $Na_{2-x}ZrO_3$:Cs^+ has more monoclinic structure phase, with secondary reflections that could be indexed to hexagonal phase with space group $P6_3$/m from its JCPDS file (as other authors have done), as well as tetragonal structure (ZrO_2) space group $P4_2$/nmc.

The ZrO_2 minor secondary phase observed at $2\theta = 30.120°$ (101) is indexed to the tetragonal phase of ZrO_2 with $P4_2$/nmc space group JCPDS card No. 79–1769. A tetragonal phase was observed by other researchers, which might be the impact of the dopant on the host matrix [7].

From the XRD patterns qualitatively, the peak intensities of the $Na_{2-x}ZrO_3$:Cs^+ phase at (200), (400), and ($\bar{3}$ 31) were observed to first decrease at the initial doping ($x = 0.05$) but were found to increase as a function of the cesium content increment. The intensity effect of cesium on the Na_2ZrO_3 family peaks at (200), (400), ($\bar{3}$ 31) could suggest the location of cesium atoms over this family plane [38]. Finally, the intensity of the tetragonal phase of ZrO_2 in Na_2ZrO_3 is indirectly proportional to the concentration of cesium [$2\theta = 30.1°$ (111)].

Na_2ZrO_3 crystallizes in the ideal $A^{2+}B^{4+}O_3^{2-}$ perovskite structure, where the A and B atoms in this case are Na and Zr atoms, respectively. The Na atom is bonded to six O^{2-} atoms forming NaO_6 octahedra which share corners with two equivalent NaO_6 octahedra, also corners with four ZrO_6 octahedra, edges with four ZrO_6 octahedra, edges with eight NaO_6 octahedra. Zr^{4+} is bonded to six O^{2-} atoms to form ZrO_6 octahedra that share corners with six NaO_6 octahedra (see the inset in Fig. 2). Applying the radius percentage difference (R_p) as

predicted by Shivakumara et al. [39], the possible site occupancy of Cs^+ in the Na_2ZrO_3 nanoparticles can be obtained:

$$R_p = \frac{R_h(CN) - R_d(CN)}{R_h(CN)} \times 100\% \qquad (2)$$

where CN is the coordination number, $R_h(CN)$ is the ionic radius of the host cation, and $R_d(CN)$ is the ionic radius of the dopant ion. The R_p between Cs^+ ion (CN = 6, $R_{Cs} = 1.67$ Å) and Na^+ ion (CN = 6, $R_{Na} = 1.02$ Å) is 64%. Similarly, the Rp for Cs^+ ion (CN = 6, $R_{Cs} = 1.67$ Å) and Zr^{4+} ion (CN = 6, $R_{Zr} = 0.72$ Å) is 132%; therefore, Cs^+ will preferentially occupy the Na^+ ion site in the Na_2ZrO_3 perovskite with lower radius percentage.

The structural characteristic of perovskite is such that it can accommodate smaller or larger ions (to a great extent) at the A-site. Goldschmidt's tolerance factor t was employed to determine the stability of $Na_{2-x}ZrO_3$:Cs^+ perovskite depending solely on the relative ionic radii of A-site cation (r_A), B-site cation (r_B), and the oxygen ion (r_0), expressed as [40]:

$$t = \frac{(r_A + r_O)}{\sqrt{2}(r_B + r_O)} \qquad (3)$$

The degree of distortion of perovskite from the ideal cubic structure from the application of tolerance factor is ($0.9 < t < 1.0$) which occurs if $0.71 < t < 0.9$ when r_A is smaller than r_B the ideal ion size [41]. The result is that the BO_6 octahedron is tilted to occupy the space not occupied by the A-site cation, so the symmetry of the crystal structure will be reduced. The tolerance factor of ABO_3 perovskite (undoped) with Na^+ substituted at the A-site is 0.807, allowing Na^+ to

Fig. 2 **A** UV–Vis absorbance and **B** optical band gap spectra of the $Cs_xNa_{2-x}ZrO_3$ perovskite
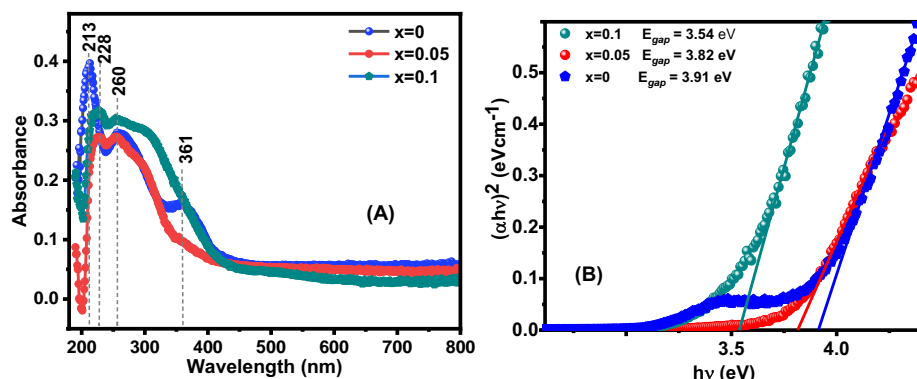
stably occupy the A-site and forming an undistorted monoclinic structure. However, when Cs^+ (CN=6, $r_{Cs}=1.67$ Å) substitutes Na^+ (CN=6, $r_{Na}=1.02$ Å) at A-site, we obtained a tolerance factor of $t = 0.916$. This affirms that Cs^+ aids in creating less distortion in the perovskite by leaving small unoccupied space at the A-site.

Rietveld refinement analysis

Specifically, when Na_2ZrO_3 is annealed at a temperature below 700 °C, it attains a monoclinic structure [37]. Conversely, when annealed at 900 °C or higher, it partially transforms into a hexagonal structure [8]. The monoclinic and hexagonal structure concentration has been analyzed qualitatively by other authors [9, 37] or semi-quantitatively using the relative intensity ratio of the JCPDF files (I_n/I_{max}) [8, 38, 42]. In the monoclinic structure, the (200) crystallographic plane exhibits an intensity of 37%, whereas the $\left(\bar{3}31\right)$ plane has an intensity of 100%. When Na_2ZrO_3 undergoes a symmetry increase, such as transitioning to a hexagonal structure, the intensity of the (200) plane also increases. In the XRD patterns, the intensity of the (200) plane surpasses 37%. Consequently, the patterns seem to indicate a dual phase consisting of both monoclinic and hexagonal symmetries. In this work, we have quantified their concentration using the Rietveld method. According to the extinction criteria, either of these space groups could be used for hexagonal symmetry: $P6_3$ (No 173), $P6_3/m$ (No. 176), or $P6_322$ (No. 182); we have concluded that the $P6_3/m$ space group could be appropriate for hexagonal symmetry in our preliminary results; however, the goodness fit of the XRD patterns has not been satisfactory. Ultimately, we have successfully fitted the XRD patterns with a satisfactory goodness of fit by employing a crystal structure that combines monoclinic and rhombohedral (hexagonal) characteristics within the $R\bar{3}m$ (166) space group, featuring hexagonal axes and lattice constants of $a=3.2435$ and $c=15.3704$ Å. Its $R\bar{3}m$ symmetry contains two molecules per cell; the Na and Cs atoms are sharing the origin site with 2/3 and 1/3, respectively; and they are in octahedral coordination with the O atoms. Table 2 enlists the atomic positions, Wyckoff site multiplicity, and occupancy of the symmetry used in this framework structure. It is seen from Fig. 1 that only the intensity of the monoclinic

Table 2 Positional parameters of the atoms in $Na_{2-x}ZrO_3$:Cs^+ perovskite with $R\bar{3}m$ symmetry

Atom	Site symmetry	Atomic coordinates			Occ
		x	y	z	
Zr	3a	0	0	0	0.6666
Na*	3a	0	0	0	0.3333
Na*	3b	0	0	0.5	1
O	6c	0	0	0.270	1

*Cs atom replaces the occupation of Na in 5 and 10%

Table 3 Quantitative results of the $Na_{2-x}ZrO_3$:Cs^+ nanocrystals by the Rietveld method

Sample		Phase concentration (wt%)				C
x	m	R	t	χ^2		(nm)
0.1	80.3	19.2	0.5	1.8		21.0
0.05	77.2	21.8	1	2.1		22.5
0	75.5	23	1.5	1.9		23.1

m monoclinic, **R** rhombohedral (Hex), t tetragonal, C average crystal size.

planes (011) and $(\bar{1}11)$ cannot be justified by the rhombohedral (Hex) structure. See the calculated XRD pattern for $Na_{2-x}ZrO_3$:Cs^+ with a rhombohedral (Hex) structure (bottom XRD pattern in the figure). In the same figure, from bottom to up are shown the profile fitting for the XRD patterns for $x=0$, $x=0.05$, and $x=0.1$. In these XRD fitting, an adequate goodness fitting for the difference between calculated and experimental data was obtained (see χ^2 factor in Table 3). As the concentration of cesium (Cs) increases within the solid solution, there is a noticeable increase in the ratio of the monoclinic phase to the rhombohedral phase (referred to as m/R). Specifically, when the Cs content reaches 10%, the concentration of monoclinic-$Na_{2-x}ZrO_3$:Cs^+ increases from 75.5 to 80.3%, while the concentration of rhombohedral-$Na_{2-x}ZrO_3$:Cs^+ decreases from 23 to 19.2%. Additionally, the refinement results indicate a reduction in the concentration of the tetragonal ZrO_2 phase from 1.5 to 0.5% (refer to Table 3). These findings suggest that the presence of Cs^+ ions has a positive effect on promoting the formation of the C 2/c monoclinic symmetry. Literature has reviewed that monoclinic Na_2ZrO_3 possesses more CO_2 capture capacity than hexagonal Na_2ZrO_3 [42].

The mean crystallite diameter size (nm) was calculated using Scherrer's formula

$$D_{hkl} = \frac{k\lambda}{\beta_{hkl}cos\theta_{hkl}} \tag{4}$$

where D_{hkl} is the crystallite size, k (Scherrer constant) is 0.9 (for spherical crystallites with cubic symmetry), λ is the wavelength (Cu = 1.5418 Å), β_{hkl} is the full width in radian at half maximum (FWHM in radians) of the peak (2θ = 16.16°, 32.41°, 33.69°, 38.82°, 55.39°, and 56.67°), and θ_{hkl} is Bragg's angle of the XRD peak. The calculated crystallite sizes are listed in Table 3 indicating a reduction of the crystallite as the Cs^+ ion concentrations increase from 23.1 to 21.0 nm.

Optical absorption energy

Figure 2A illustrates the optical absorbance spectra of the $Na_{2-x}ZrO_3$:Cs^+ nanocrystals synthesized at room temperature. These spectra offer valuable insights into the material's energy band gap, transition processes, and band positions. Within the ultraviolet region, distinctive absorption bands are observed, arising from electron transitions from the valence to the conduction bands within the nanomaterials. Specifically, for samples within the range of $0 \leq x \leq 0.1$, synthesized with varying Na/Cs molar ratios in the precursors, the absorption edges were found at wavelengths of 213 nm, 260 nm, and 361 nm for the pure sample. The introduction of Cs^+ ions into the host matrix induced a shift in the absorption band from 213 to 228 nm and the disappearance of the 361 nm absorption band in all the doped samples. To calculate the energy band gap, we employed Wood and Tauc's expression (Eq. 5) in conjunction with the Kubelka–Munk (K-M) equation.

$$hv\alpha \propto (hv - E_g)^m \tag{5}$$

where E_g is the optical band gap, $\propto$ is the linear absorption coefficient of the sample, h is the Planck constant, v is the frequency, hv the photon energy, and m is a constant depending on the nature of transition (m = 1/2, 3/2, 2, or 3 for direct allowed, direct forbidden, indirect allowed, or indirect forbidden transitions, respectively).

Kubelka–Munk (K-M) function $F(R_\infty)$ Eq. (6) is used to transform the diffuse reflectance spectrum into its absorption equivalent.

$$F(R_\infty) = \frac{A}{S} = \frac{(1 - R_\infty)^2}{2R_\infty} \tag{6}$$

where $R_\infty = \frac{R_{sample}}{R_{standard}}$ is the reflectance R of an infinitely thick specimen, while A and S are the K-M absorption and scattering coefficients. Substituting Eq. (6) into Eq. (5) gives Eq. (7):

$$\left[F(R_\infty)hv\right]^{1/2} = C(hv - E_g) \tag{7}$$

Tauc's plot, generated by plotting $\left[F(R_\infty)hv\right]^{1/2}$ against photon energy hv, allows for the extrapolation of the band gap (E_g) by fitting a straight line to the linear or steepest section of the absorption rise between inter-band transitions where it intersects the hv axis [43, 44]. The extrapolated indirect band gap energies are 3.92 eV, 3.82 eV, and 3.55 eV, corresponding to wavelengths of 316 nm, 325 nm, and 349 nm, respectively (see Fig. 3B). These findings demonstrate that by adjusting the Na/Cs molar ratios in the precursors, the band gap energies of $Na_{2-x}ZrO_3$:Cs^+ perovskite can be continuously varied from 316 to 349 nm, thereby expanding the range of optical absorption into the visible light spectrum. The blue shift in the band gap of nanoparticles is a result of the quantum confinement effect [45, 46].

Scanning electron microscopy (SEM) analysis

Scanning electron microscopy (SEM) techniques were utilized to examine the microstructures, including elemental composition, morphology, and mapping, of the samples as illustrated in Fig. 3 (labeled as A_1, B_1, and C_1). The average particle sizes determined from the SEM images were 184 nm, 223 nm, and 247 nm, exhibiting an increasing trend with higher dopant concentrations. The particle size distribution histograms are presented in Fig. 3 (labeled as A_3, B_3, and C_3) for each sample, respectively.

The significant porosity observed in these nanomaterials can be attributed to the increased release of gases during the annealing process. The use of nitrate precursors facilitates the liberation of substantial amounts of nitrogen-containing gases at high annealing temperatures, contributing to the formation
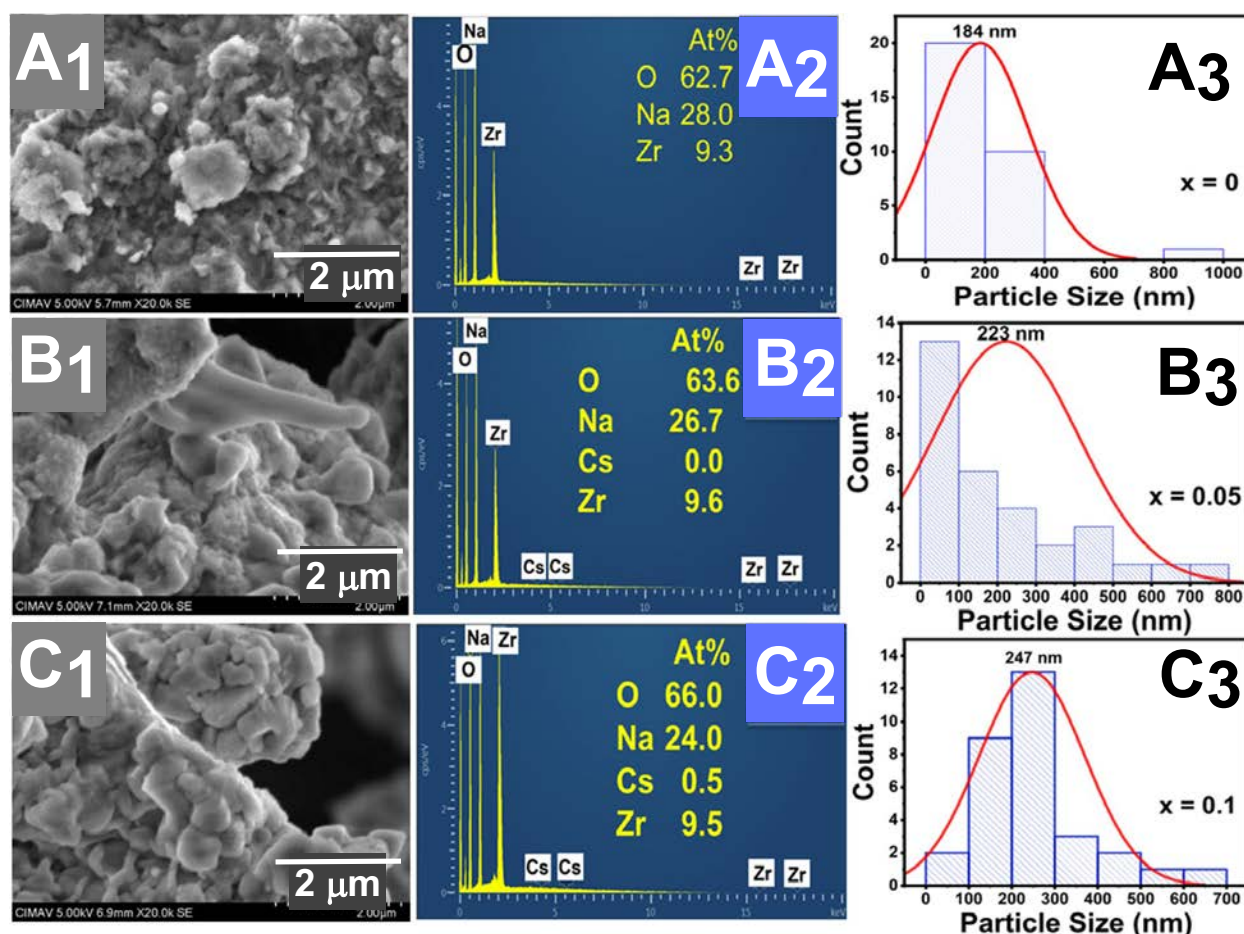
Fig. 3 SEM micrograph, EDS spectra, and particle size histogram: A_1, A_2, A_3 for $x = 0$; B_1, B_2, B_3 for $x = 0.05$; C_1, C_2, C_3 for $x = 0.1$ of $Na_{2-x}ZrO_3$:Cs^+ perovskite nanomaterials

of a porous structure. These pores are irregular in shape due to gaps forming within the fluffy walls of the nanomaterials. In contrast, the undoped sample exhibits a denser and more compacted fluffy structure. Importantly, there were no observable changes in the nanoparticle morphology as a result of varying Cs^+ ion concentrations.

Analysis of the energy-dispersive X-ray spectroscopy (EDS) spectra (refer to Fig. 3, labeled as A_2, B_2, C_2) revealed the presence of elements such as sodium (Na), zirconium (Zr), cesium (Cs), and oxygen (O) in all three samples. The major peak emission energies were as follows: sodium (Na) at 1.040 keV ($k\alpha 1$), zirconium (Zr) ranging from 2.044 keV ($L\alpha_1$) to 2.126 keV ($L\beta_1$), cesium (Cs) ranging from 4.285 keV ($L\alpha_1$) to 4.619 keV ($L\beta_1$). Notably, in the $x = 0.05$ sample, there were no emission spectra

observed for cesium (Cs), which could be attributed to its evaporation at high temperatures during the annealing process. Furthermore, oxygen (O) was detected at 0.525 keV ($k\alpha_1$). Importantly, no impurities were detected in any of the synthesized samples, and the atomic percentages of the elements were found to be consistent with the stoichiometric

Table 4 Elemental composition of $Cs_xNa_{2-x}ZrO_3$ perovskite nanoparticles determined by EDSA-SEM analysis

Elements	$x = 0$ At%	$x = 0.05$ At%	$x = 0.1$ At%
O^{2-}	62.7	63.6	66.0
Na^+	28.0	26.7	24.0
Cs^+	****	0.0	0.5
Zr^{4+}	9.3	9.6	9.5

composition (please refer to Table 4). Additionally, when examining the nanoparticle micrograph for the $x=0$ sample, the mapping results demonstrated a homogeneous distribution of sodium (Na) and zirconium (Zr) (as depicted in Fig. 4).

High-resolution transmission electron microscopy (HRTEM)

High-resolution transmission electron microscopy (HRTEM) was obtained at 200 kV for the samples. These samples (Fig. 5A₂, B₂) show a distribution of spherical nanocrystallites with well-defined diffraction fringes. The interplanar spacings measured at $x=0$ and $x=0.05$ are 0.284 nm and 0.273 nm, respectively, representing a monoclinic structure according to the JCPDS card No. 35–0770. The HRTEM images (Fig. 5A₁, B₁) of the nanocrystals are consistent with the data calculated by X-ray diffraction within 20 nm.

Raman spectroscopy and FTIR analysis

Raman spectroscopy is a technique used for identifying the crystal symmetry and different polymorphs of metal oxides. According to group theory, specific crystalline phases such as monoclinic, tetragonal, and cubic are expected to exhibit distinct Raman spectra [47, 48]. In the case of Cs-doped Na_2ZrO_3 nanocrystals, a Raman spectrum was recorded in the 200–850 cm⁻¹ range at room temperature, as depicted in Fig. 6. The interpretation of the observed bands was based on prior research [49–51]. For the m-ZrO_2 crystalline phase, the vibrational Raman active modes are described as $\Gamma = 9A_g + 9B_g$. In the A_g mode, oxygen atoms only move in the z-direction, while in the B_g mode, both Zr and O atoms contribute to motion in the z-direction. Upon analyzing these spectra from Na_2ZrO_3:Cs^+ nanocrystals, it is evident that the samples display multiple peaks positioned at different wavenumbers, which are detailed in Table 5. The deconvoluted spectra reveal that there are 15 bands present in the Raman spectra within the 200 to 850 cm⁻¹ spectral range for the undoped sample. However, in the doped samples, only eight bands are observed. This reduction in the number of bands in the doped samples can be attributed to the low polarizabilities of certain modes and slight distortions in the Na_2ZrO_3 crystal, which ultimately diminish spectral resolution. Consequently, providing a clear and definitive assignment for these bands becomes a complex task.

The rate of radiative transitions within the nanocrystal materials was examined to estimate the phonon energy through the Lorentzian fitting on each of the examined Raman spectra; the representative figures are depicted in Fig. 7. The Lorentzian fitting of the spectrum revealed 11 phonon bands centered and 7 phonon bands for the doped samples, respectively. Taking into account the positions (x_i), FWHMs (w_i), and the intensities (A_i) of the corresponding Lorentzian subbands, the effective phonon energy for the present nanocrystal was estimated by applying Eq. (8) considering the positions (x_i), FWHMs (w_i), and the intensities (A_i) of the corresponding Lorentzian subbands [51, 52].

$$E_{ph} = \frac{\sum_i x_i w_i A_i}{\sum_i w_i A_i} \tag{8}$$

The calculated values of the effective phonon energies are 436, 434, and 433 cm⁻¹ for $x=0$, $x=0.05$, and $x=0.1$, respectively. The obtained phonon energies for the samples under review are lower in values as in comparison to the previously reported for ZrO_2
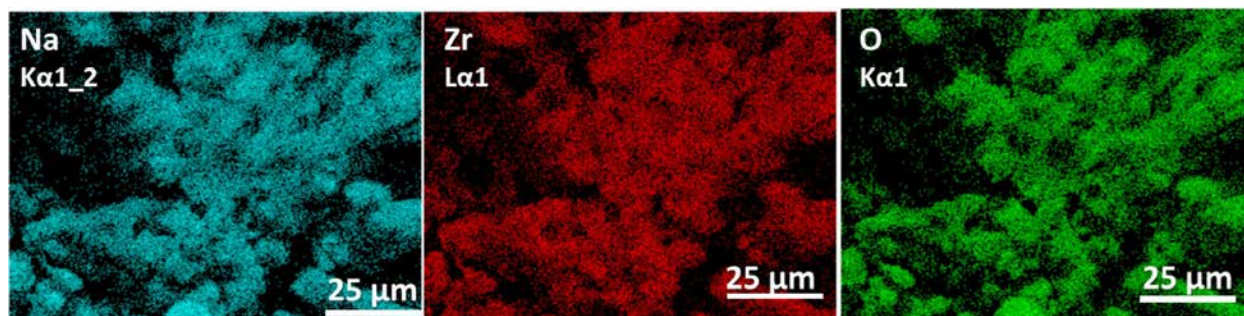

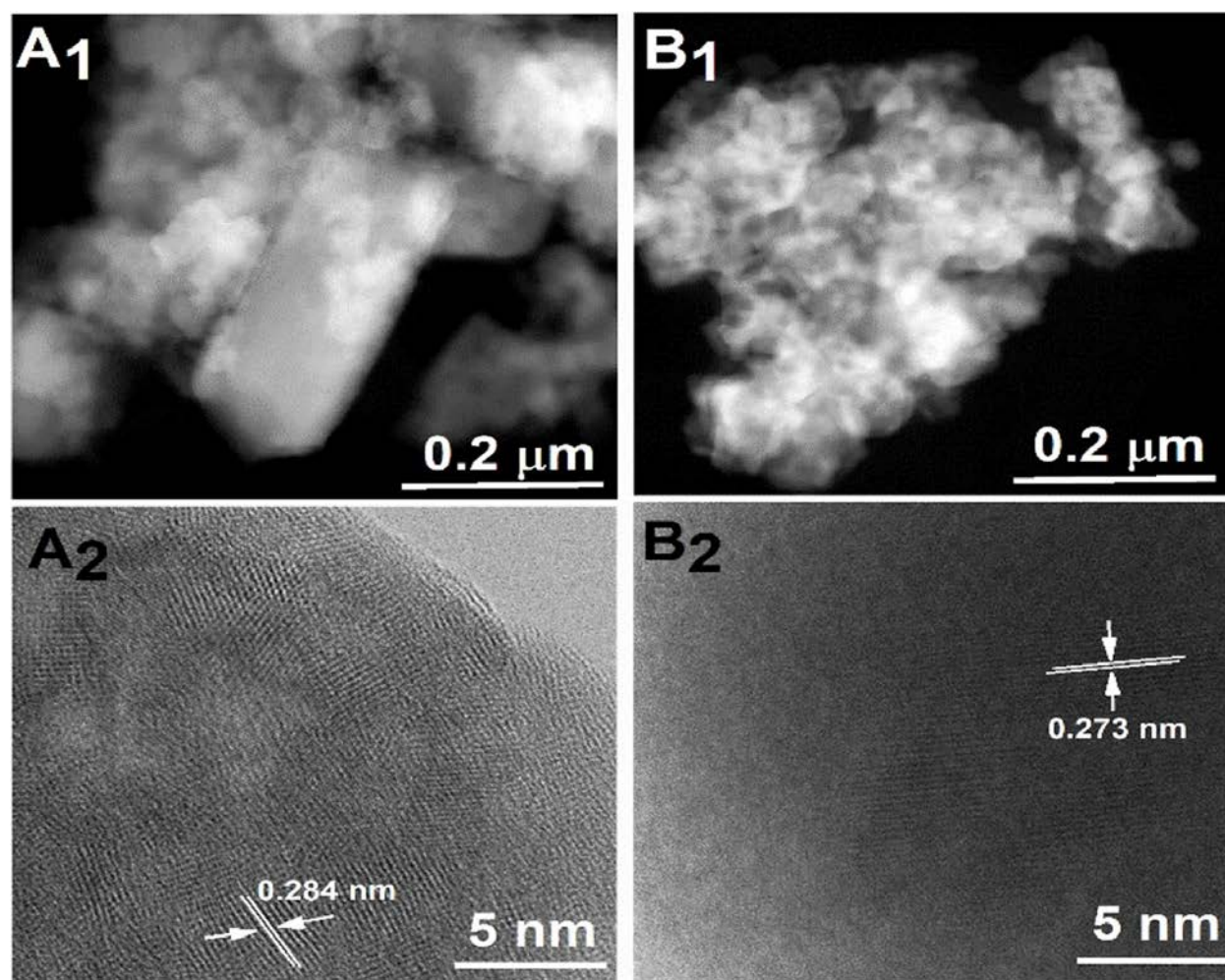**Fig. 4** Mapping of $x=0$ sample of $Cs_xNa_{2-x}ZrO_3$ perovskite nanoparticles

Fig. 5 TEM micrograph ($\mathbf{A_1}$, $\mathbf{B_1}$) and HRTEM ($\mathbf{A_2}$, $\mathbf{B_2}$) for $x=0$ and $x=0.05$ of $Na_{2-x}ZrO_3$: Cs^+

matrix (442 cm^{-1}; 443, 445 cm^{-1}) [51, 52]. Low phonon energies help reduce the likelihood of nonradiative multiphonon relaxation of excited activator ions within the vibrational bands of the nanomaterial's host lattice. Therefore, it can be inferred that the current nanocrystals ($Na_2ZrO_3:Cs^+$) possess the properties required for photonic applications.

Figure 6 shows the FTIR spectra of the Cs-doped Na_2ZrO_3 and the undoped sample ($x=0$). All the samples exhibit the metal–oxygen vibrations of Na–O and Zr-O between 400 and 750 cm^{-1} which were also reported by other researchers [53, 54]. The vibrational band at 488 cm^{-1} corresponds to the infrared spectrum of ZrO_2 phase [55]. The two main observed vibration modes at~ 879 cm^{-1} and~ 1417 cm^{-1} correspond to the Na–O bending mode and oxalate

vibrational frequency in Na_2ZrO_3. This could also be attributed to nitrate groups found in the used precursors [54]. The peak observed at 2342 and 2156 cm^{-1} is associated to the coupling effect of –OH groups stretching and bending vibrations. The band observed at 1975 cm^{-1} is due to O=H bonding. The absence of a peak at~ 3000 cm^{-1} indicates that adsorbed (H–O-H) molecules have been successfully removed during heat treatment.

Carbonation kinetic study of $Na_{2-x}ZrO_3:Cs^+$ sorption

The study of the kinetics of carbon dioxide adsorption by perovskite-type metal oxides is important because it can provide deeper insights into the possibilities of using the material as an adsorbent for air separation or as a
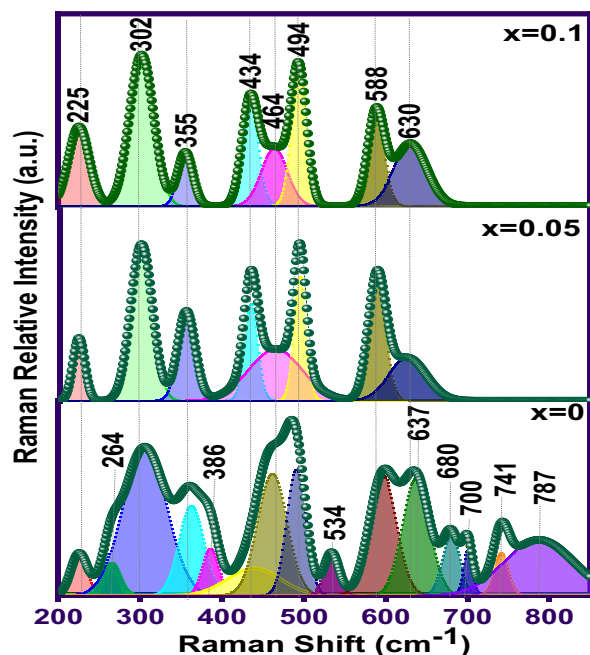
Fig. 6 De-convoluted Raman spectra for pure and Cs-doped Na_2ZrO_3

reaction membrane for methane conversion. The thermal property of the $Na_{2-x}ZrO_3$:Cs^+ perovskite nanocrystal dried gel was studied by a simultaneous thermogravimetric and differential scanning calorimetry analysis

(TGA–DSC) under air flow. This thermal analysis procedure is used to determine the temperature at which a nitrate matrix decomposes and crystallizes without further weight loss. As shown in Fig. 9, the TGA curve shows the sequence of steps (depending on the sample) that includes different mass loss steps such as dehydration and decarboxylation. When the Cs concentration is $x=0$, 0.05, and 0.1, the initial weight loss below 200 °C is 2.72%, 4.47%, and 5.58%, respectively. The difference in Cs concentration is attributed to the release of absorption solvents such as water and acetic acid. The weight loss in the second stage (77.48%, 71.91%, and 66.82%, respectively) with increasing temperature was due to the thermal decomposition of zirconium acetate, sodium nitrate, and cesium nitrate. The pure ($x=0$) sample shows a faster decomposition rate and more weight loss in comparison to the Cs^+-doped samples. The residue with higher stability is 19.8% for pure cesium concentration, 23.6% for cesium concentration $x=0.05$, and 27.6% for cesium concentration $x=0.1$. This validates the effects of Cs^+ incorporation in the Na^+ site with an enhanced and sustained stability of the perovskite from faster decomposition and weight loss. The TGA curves of the three samples reviewed were very steep, indicating that some species (e.g., water, organic material) evaporated from the samples. The DSC curve also steepens at these various ranges of the TGA, and the

Table 5 Raman phonon frequency modes for Na_2ZrO_3:Cs^+ under study

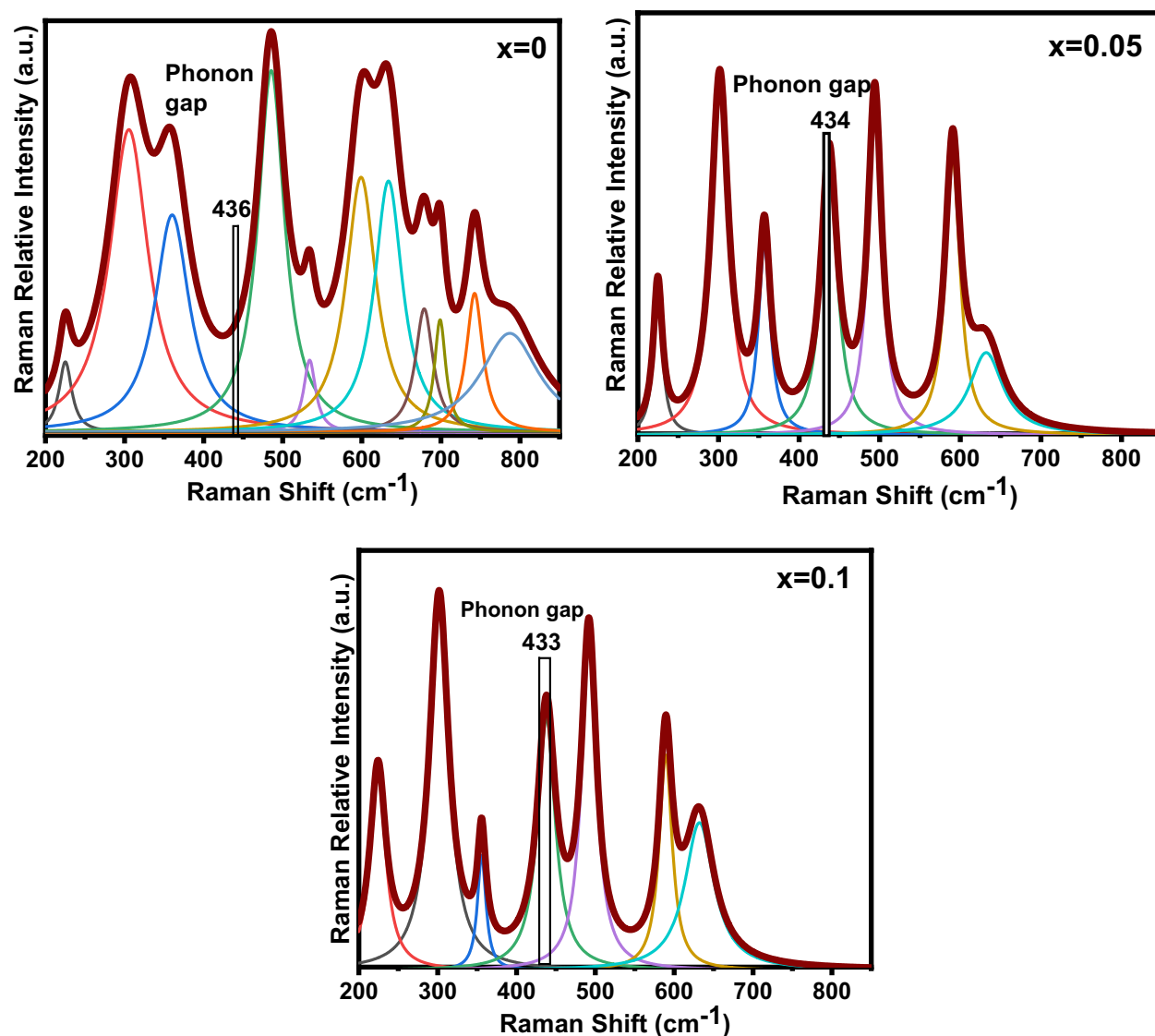|	$X=0$ Frequencies (cm^{-1})	$X=0.05$ Frequencies (cm^{-1})	$X=0.1$ Frequencies (cm^{-1})	Raman symmetry
1	225.142	225.142	225.142	A_g
2	264.159	-	-	A_g
3	305.466	301.72	301.72	B_g
4	362.661	355.225	355.225	B_g
5	386.153	-	-	A_g
6	439.046	434.141	434.141	B_g
7	461.072	463.516	463.516	A_g
8	490.338	493.988	493.988	A_g
9	534.015	-	-	Bg
10	596.638	588.241	588.241	B_g
11	637.292	630.135	630.135	A_g
12	680.085	-	-	A_g
13	700.203	-	-	B_g
14	741.445	-	-	B_g
15	787.12	-	-	B_g

Fig. 7 Lorentzian fitting of Raman spectra for pure and Cs-doped Na_2ZrO_3

extreme value of the DSC curve is 450 °C, 644 °C, and 724 °C for $x=0$, $x=0.05$, and $x=0.1$ concentration, respectively, suggesting that organic materials in these samples decompose at those temperatures.

Figure 10a illustrates the CO_2 adsorption behavior of $Na_{2-x}ZrO_3:Cs^+$ in a pure CO_2 stream at 700 °C and 1 bar. From the TGA cyclic stability sorption of $Na_{2-x}ZrO_3:Cs^+$ sorption over two cycles at sorption temperature of 500 °C and 700 °C regeneration graphically depicted in Fig. 11a–d, $Na_{1.9}Cs_{0.1}ZrO_3$ sample has higher adsorption capacity with faster adsorption kinetics, followed by $Na_{1.95}Cs_{0.05}ZrO_3$ as compared to the

pure Na_2ZrO_3 sample. The maximum CO_2 adsorption for cesium concentrations ($x=0.1$ and 0.05) was reached in 10 min are 11.45 wt% and 9.7 wt%, respectively, which was slightly higher than that for Na_2ZrO_3 (8.08 wt%). At 120 min, more weight loss due to CO_2 adsorption was still observed in the spectra. There is a gradual increase of sorption and regeneration conversion with Cs content increment in the first cycle and second regeneration, respectively, but the lower sorption and regeneration conversion at the second sorption and first regeneration for $x=0.05$ samples (see Table 6). Maximum observed CO_2 sorption conversion and kinetics for the first and
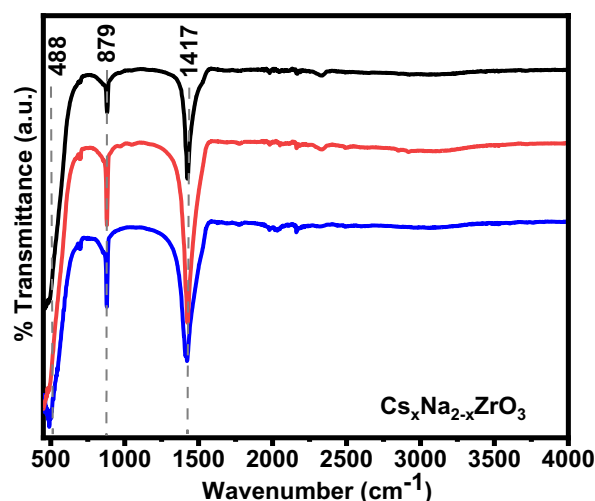
Fig. 8 FTIR of $Na_{2-x}ZrO_3:Cs^+$ perovskite nanocrystals

second cycle as observed from Table 6 and Fig. 11 for $x=0.1$ sample is a 9.044% and 13.01% conversion, which is higher over the non-doped Na_2ZrO_3 ($x=0$). Regeneration conversions showed a maximum of 13.04% mol of Cs impacts.

The obtained CO_2 sorption capacity of $Na_{2-x}Cs_xZrO_3$ is higher than the 11% sorption capacity obtained by Da et al. [25] in their publication on Li-doped Na_2ZrO_3. But these results are lower than the theoretical CO_2 sorption capacity of 23.8 wt%, which could be a result of (a) unreacted precursors, (b) high-temperature treatment sintering, (c) the presence of secondary t-ZrO_2 phase with no CO_2 sorption capacity, and (d) the use of all-inorganic precursors [57]. High-temperature sintering changes the mesoporosity of the Na_2CO_3/ZrO_2 shell, leading to low diffusion of the CO_2 adsorption
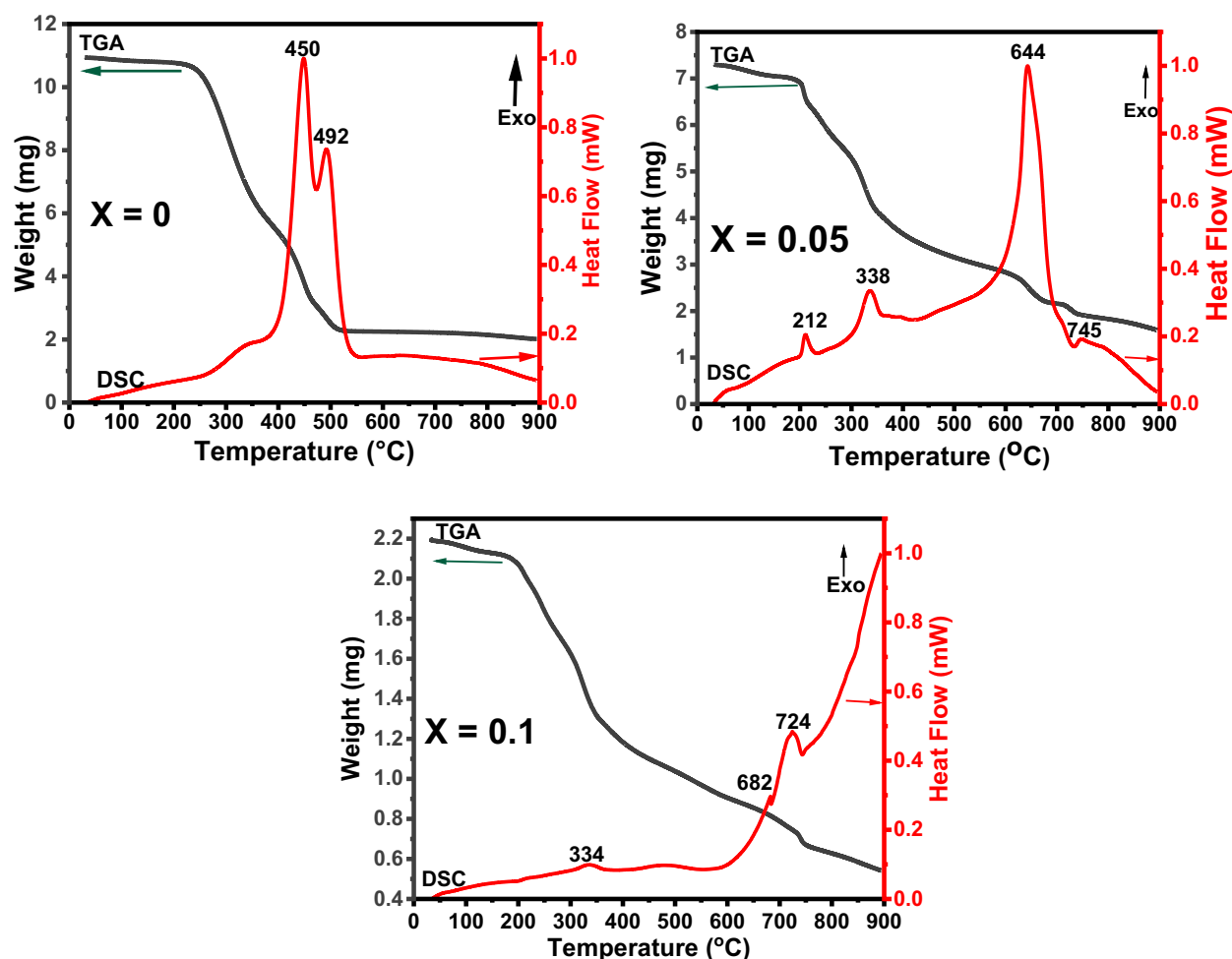

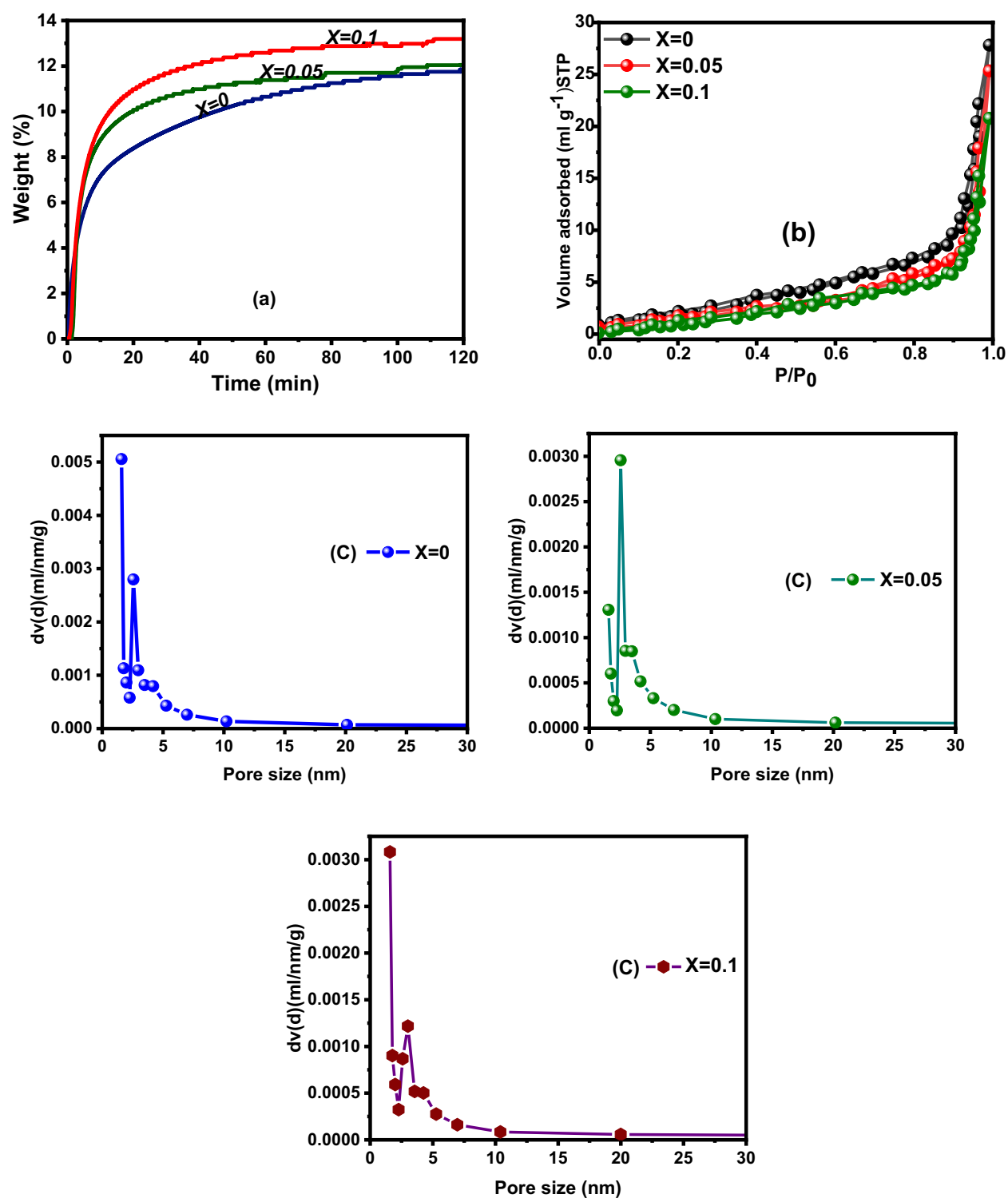**Fig. 9** TGA/DSC curves of $Na_{2-x}ZrO_3:Cs^+$ nanocrystals

Fig. 10 a Sorption at 700 °C, 1 bar in pure CO_2 flow, **b** N_2 adsorption–desorption isotherms, **c** pore size distribution for $Na_{2-x}ZrO_3:Cs^+$ sorption

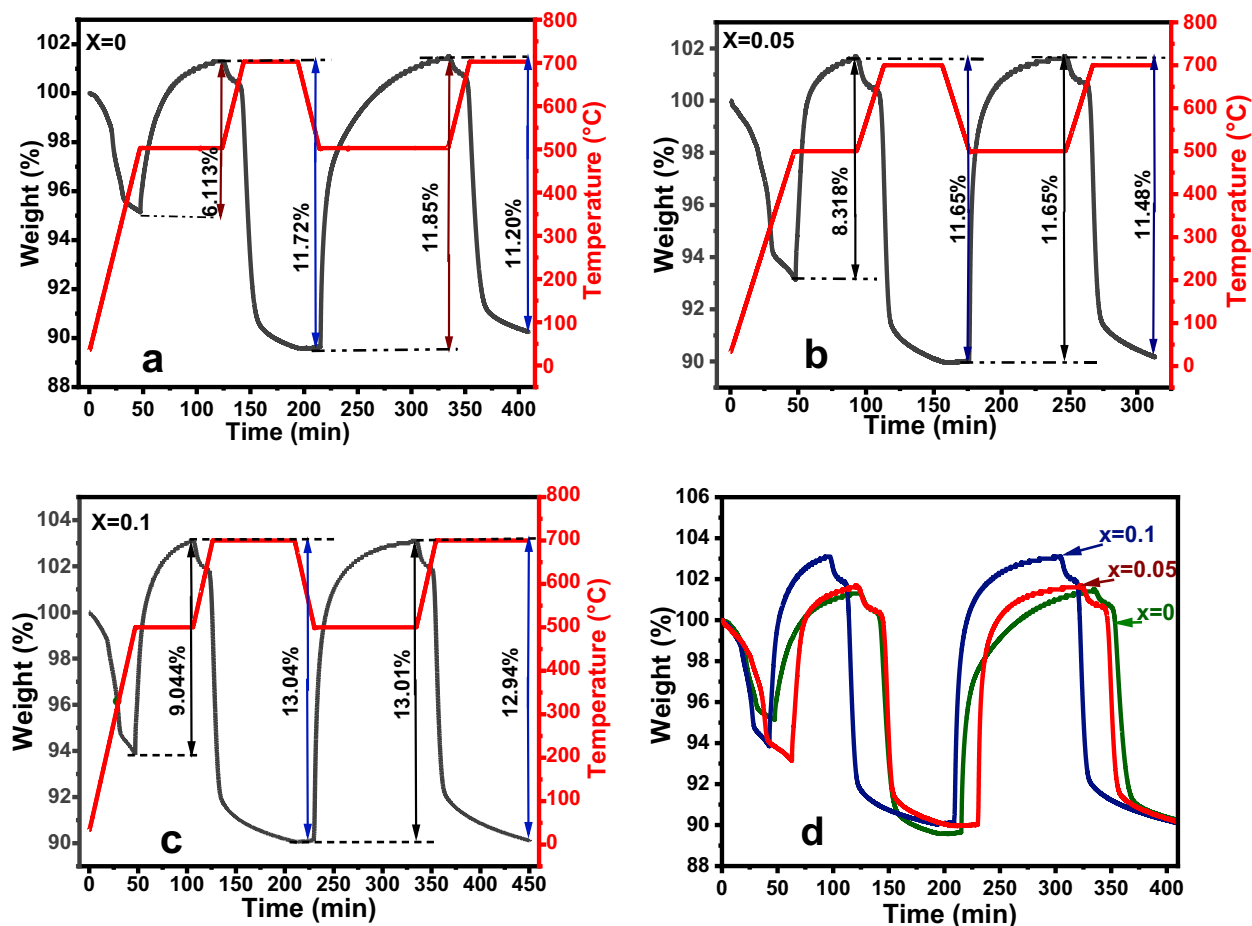**Fig. 11** TGA cyclic stability sorption of $Na_{2-x}ZrO_3:Cs^+$ sorption over two cycles at sorption temperature of 500 °C and 700 °C regeneration

Table 6 Sorption-regeneration data

Samples	1st cycle		2nd cycle	
	Sorption (%)	Regeneration (%)	Sorption (%)	Regeneration (%)
$X=0$	6.1	11.7	11.9	11.2
$X=0.05$	8.3	11.6	11.7	11.5
$X=0.1$	9.0	13.0	13.0	12.9

Table 7 Surface area, pore size, and pore volume of $Na_{2-x}ZrO_3:Cs^+$ sorbent

Samples	BET surface area (m^2g^{-1})	Average pore diameter (nm)	Pore volume (mlg^{-1})
$X=0$	9.2	3.5	0.4
$X=0.05$	9.5	4.3	0.5
$X=0.1$	15.1	3.1	0.6

process on Na_2ZrO_3 [56]. The enhanced CO_2 sorption kinetic is a result of Cs (with the formation of Cs_2ZrO_3) substitution and compensating part of the Na in the host matrix Na_2ZrO_3, thus resulting in more sorption capture. This response means that the adsorption kinetics of Cs_2ZrO_3 may be faster than that of Na_2ZrO_3 if such a study could be conducted.

The optical absorbance spectra of the as-synthesized for the specific surface area, pore size, and pore volume of the sorbent employed for all the samples are shown in Fig. 10b, which presented type II isothermal material characteristics with a wide range of pore sizes. The BET surface area, average pore diameter, and pore volume of the sorbent with adsorption and desorption isotherm obtained values are summarized in Table 7. The

pure sample was observed to be more porous than the Cs^+ ion doped whose porosity decreases with increased concentration. This confirms the faster decomposition of the pure sample. The surface areas of Cs^+-doped BETs differ slightly from each other. Figure 10c is a graph depicting the pore size distributions of the three samples; the pure sorbent shows fewer pores of 3.092 nm (diameter), while the sorbents with Cs^+ concentrations of 0.05 and 0.1 showed larger pore sizes. It is usual that the particles having smaller pores also have a larger specific surface area but the surface area of one gram of particles depends also on the number of pores is in that particle, i.e., the specific surface area of a particle is a function of porosity. As the size of a nanoparticle decreases, its surface-area-to-volume ratio increases, leading to increased surface reactivity (physical and chemical properties). The increased surface area also results in a higher number of active sites for chemical reactions and a greater potential for interaction with carbon dioxide gas, enabling more adsorption. On the other hand, as the size increases, the surface-area-to-volume ratio decreases, leading to a decrease in CO_2 adsorption.

A dense particle (the pure sorbent) creates an insufficient medium with increased pressure in the medium particle for the release of gas generated from decomposition. When oxalate and nitrate precursors are annealed at a defined temperature and atmosphere, gaseous products are generated, and thus, the release of gas creates void spaces in the material. The pore distribution shown in Fig. 10c indicates that the majority of the analyzed adsorbent materials consist mainly of mesopores [59]. Increasing the surface area of the adsorbent gives rise to an increase in the adsorption of gases. This response is because the increased surface area provides a greater number of adsorption sites. It thus suggests that Cs^+-doped Na_2ZrO_3 material is an efficacious CO_2 sorption material when the already listed limitations in regard to the annealing temperature, the use of carbonate-based reagents in place of nitrate-based chemical sources, and a diligent synthesis route to eliminate the secondary phase.

Conclusion

In this study, we successfully synthesized cesium-doped sodium zirconate perovskite nanocrystals using a sol–gel method. The structural analysis reveals the predominant monoclinic phase with a weak tetragonal secondary phase. The calculated crystal size is ~20 nm. The optical spectra reveal a strong absorption band from the electronic transition from valance to conduction band with a decrease in the optical band gap from 3.91 to 3.54 eV with increasing cesium concentration. The calculated effective phonon energies inferred that $Na_2ZrO_3:Cs^+$ nanocrystals possess the properties required for photonic applications. CO_2 adsorption results demonstrated fast adsorption kinetics and sufficient carbonation capacity. The results validate that $Na_2ZrO_3:Cs^+$ nanocrystal perovskites are good materials for photonic and photocatalytic applications.

Declarations

Conflict of interest   The authors declare no competing interests.

References

1. Abdel-Aal SK, Abdel-Rahman AS (2020) Graphene influence on the structure, magnetic, and optical properties of rare-earth perovskite. J Nanopart Res 22:267–310

2. Khine EE, Koncz-Horvath D, Kristaly F et al (2022) Synthesis and characterization of calcium oxide nanoparticles for CO_2 capture. J Nanopart Res 24:39–11

3. Kumar A, Manam, J (2020) Red emitting Eu^{3+} doped Na_2ZrO_3 phosphor with high color purity for w-LED applications. AIP Conf Proc 2220:080005–6

4. Kumar A, Manam J (2021) Thermally stable Na_2ZrO_3: Eu^{3+} phosphors for UV excited tricolor white LEDs. Mater Today Proc 46:6107–6112

5. Santiago-Torres N, Romero-Ibarra IC, Pfeiffer H (2014) Sodium zirconate (Na_2ZrO_3) as a catalyst in a soybean oil transesterification reaction for biodiesel production. Fuel Process Technol 120:34–39

6. de Lima JR, O, et al (2012) Strontium zirconate heterogeneous catalyst for biodiesel production: synthesis, characterization and catalytic activity evaluation. Appl Catal A Gen 445(446):76–82

7. Munro S, Åhlén M, Cheung O, Sanna A (2020) Tuning Na_2ZrO_3 for fast and stable CO_2 adsorption by solid state synthesis. Chem Eng J 388:124284–124313

8. Zhao T, Rønning M, Chen D (2013) Preparation of nanocrystalline Na_2ZrO_3 for high-temperature CO_2

acceptors: chemistry and mechanism. J Energy Chem 22:387–393

9. Zhao T, Ochoa-Fernández E, Rønning M, Chen D (2007) Preparation and high-temperature CO_2 capture properties of nanocrystalline Na_2ZrO_3. Chem Mater 19:3294–3301

10. Pires JCM, Martins FG, Alvim-Ferraz MCM, Simões M (2011) Recent developments on carbon capture and storage: an overview. Chem Eng Res Des 89:1446–1460

11. Jo HG, Yoon HJ, Lee CH, Lee KB (2016) Citrate sol–gel method for the preparation of sodium zirconate for high-temperature CO_2 sorption. Ind Eng Chem Res 55:3833–3839

12. Tangsathitkulchai C, Naksusuk S, Wongkoblap A, Phadungbut P, Borisut P (2021) Equilibrium and kinetics of CO_2 adsorption by coconut shell activated carbon impregnated with sodium hydroxide. Processes 9(201):2–23

13. Yoon HJ, Lee KB (2019) Introduction of chemically bonded zirconium oxide in CaO-based high-temperature CO_2 sorbents for enhanced cyclic sorption. Chem Eng J 355:850–857

14. Kwon S, Lee SG, Chung E, Lee WR (2015) CO_2 adsorption on H_2O-saturated BaO(100) and induced barium surface dissociation. Bull Korean Chem Soc 36:11–16

15. Elvira G-B, Francisco G-C, Víctor S-M, Alberto M-LR (2017) MgO-based adsorbents for CO_2 adsorption: influence of structural and textural properties on the CO2 adsorption performance. J Environ Sci 57:418–428

16. Li L, Shi Z, Gao B, Hu X, Wang Z (2016) Electrochemical conversion of CO_2 to carbon and oxygen in $LiCl–Li_2O$ melts. Electrochim Acta 190:655–658

17. Nair S, Raghavan R (2021) A kinetic study of CO_2 sorption/desorption of lithium silicate synthesized through a ball milling method. Thermochim Acta 699:178918–179010

18. Rangwala HA (1996) Absorption of carbon dioxide into aqueous solutions using hollow fiber membrane contactors. J Memb Sci 112:229–240

19. Xiong R, Ida J, Lin YS (2003) Kinetics of carbon dioxide sorption on potassium-doped lithium zirconate. Chem Eng Sci 58:4377–4385

20. Pfeiffer H, Lima E, Bosch P (2006) Lithium−sodium metazirconate solid solutions, $Li_{2-x}Na_xZrO_3$ ($0 \leq x \leq 2$): a hierarchical architecture. Chem Mater 18:2642–2647

21. Xiao Q, Liu Y, Zhong Y, Zhu W (2011) A citrate sol–gel method to synthesize Li_2ZrO_3 nanocrystals with improved CO_2 capture properties. J Mater Chem 21:3838–3842

22. Alcérreca-Corte I, Fregoso-Israel E, Pfeiffer H (2008) CO2 absorption on Na2ZrO3: a kinetic analysis of the chemisorption and diffusion processes. J Phys Chem C 112:6520–6525

23. Radfarnia HR, Iliuta MC (2012) Application of surfactant-template technique for preparation of sodium zirconate as high temperature CO_2 sorbent. Sep Purif Technol 93:98–106

24. Ooi KM, Chai SP, Mohamed AR, Mohammadi M (2015) Effects of sodium precursors and gelling agents on CO_2 sorption performance of sodium zirconate. Asia-Pacific J Chem Eng 10(4):565–579

25. Barraza-Jiménez D, Collins-Martínez V, Reyes-Rojas A, Guzmán-Velderráin V, López-Ortiz A (2004) The effect of Li as a dopant in Na2O3Zr high temperature CO_2

acceptor. https://folk.ntnu.no/skoge/prost/proceedings/aiche-2004/pdffiles/papers/263d.pdf. Accessed 12 October 2023

26. Centi G, Quadrelli EA, Perathoner S (2013) Catalysis for CO_2 conversion: a key technology for rapid introduction of renewable energy in the value chain of chemical industries. Energy Environ Sci 6:1711–1731

27. Nathanael AJ, Kannaiyan K, Kunhiraman AK, Ramakrishna S, Kumaravel V (2021) Global opportunities and challenges on net-zero CO_2 emissions towards a sustainable future. React Chem Eng 6:2226–2247

28. Salvi BL, Jindal S (2019) Recent developments and challenges ahead in carbon capture and sequestration technologies. SN Appl Sci 1:885–920

29. Global Monitoring Laboratory (2021) Earth system research laboratories trends in atmospheric carbon dioxide. https://gml.noaa.gov/ccgg/trends/. Accessed 12 October 2023

30. Paramsothy M (2020) Alleviating climate change and pollution with nanomaterials. Nanomaterials 10:358–362

31. Leonzio G, Zondervan E, Foscolo PU (2019) Methanol production by CO_2 hydrogenation: analysis and simulation of reactor performance. Int J Hydrogen Energy 44:7915–7933

32. Cui X, Kær SK (2020) A comparative study on three reactor types for methanol synthesis from syngas and CO_2. Chem Eng J 393:124632–124711

33. Sorcar S et al (2019) CO_2, water, and sunlight to hydrocarbon fuels: a sustained sunlight to fuel (Joule-to-Joule) photoconversion efficiency of 1%. Energy Environ Sci 12:2685–2696

34. Zhang Y et al (2019) Recent advances in lithium containing ceramic based sorbents for high-temperature CO_2 capture. J Mater Chem A 7:7962–8005

35. Hao G-P, Li W-C, Lu A-H (2011) Novel porous solids for carbon dioxide capture. J Mater Chem 21:6447–6451

36. Wang J et al (2014) Recent advances in solid sorbents for CO_2 capture and new development trends. Energy Environ Sci 7:3478–3518

37. Bastow TJ, Hobday ME, Smith ME, Whitfield HJ (1994) Structural characterisation of Na_2ZrO_3. Solid State Nucl Magn Reson 3:49–57

38. Sandoval-Diaz A, Pfeiffer H (2008) Effects of potassium doping on the composition, structure and carbon dioxide chemisorption of Na_2ZrO_3. Rev Mex física 54:65–68

39. Shivakumara C, Saraf R, Halappa P (2016) White luminescence in Dy^{3+} doped BiOCl phosphors and their Judd-Ofelt analysis. Dye Pigment 126:154–164

40. Goldschmidt VM (1927) Krystallbau und chemische Zusammensetzung. Berichte der Dtsch Chem Gesellschaft (A B Series) 60:1263–1296

41. Li Z et al (2016) Stabilizing perovskite structures by tuning tolerance factor: formation of formamidinium and cesium lead iodide solid-state alloys. Chem Mater 28:284–292

42. Ji G, Memon MZ, Zhuo H, Zhao M (2017) Experimental study on CO_2 capture mechanisms using Na_2ZrO_3 sorbents synthesized by soft chemistry method. Chem Eng J 313:646–654

43. Jubu PR et al (2022) Dispensability of the conventional Tauc's plot for accurate bandgap determination from

UV–vis optical diffuse reflectance data. Results Opt 9:100273–100277

44. Kalu O et al (2023) Structural and optical characterization of RF sputtered CdMgZnO thin film with different Cd concentrations. Mater Chem Phys 308:128314–128411

45. Kaviyarasu K, Devarajan PA, Xavier SSJ, Thomas SA, Selvakumar S (2012) One pot synthesis and characterization of cesium doped SnO_2 nanocrystals via a hydrothermal process. J Mater Sci Technol 28:15–20

46. Asha A B, Narain R (2020) Nanomaterials properties. In: Narain R (ed) Polymer science and nanotechnology, 1st edn. Elsevier, Canada, pp 343–359

47. Singh KA, Pathak LC, Roy SK (2007) Effect of citric acid on the synthesis of nano-crystalline yttria stabilized zirconia powders by nitrate–citrate process. Ceram Int 33:1463–1468

48. Zhang J et al (2018) Oxygen vacancy-rich mesoporous ZrO_2 with remarkably enhanced visible-light photocatalytic performance. Sol Energy Mater Sol Cells 182:113–120

49. Reddy CV, Babu B, Reddy IN, Shim J (2018) Synthesis and characterization of pure tetragonal ZrO_2 nanoparticles with enhanced photocatalytic activity. Ceram Int 44:6940–6948

50. Shkerin SN et al (2021) Raman spectroscopy of $SrZrO_3$ based proton conducting electrolyte: effect of Y-doping and Sr-nonstoichiometry. Int J Hydrogen Energy 46:17007–17018

51. Nathan-Abutu A, Ahemen I, Reyes-Rojas A (2023) Structural and optical investigation of novel $Sr_{1-x}Na_{2x}ZrO_3$ perovskite nanoparticles. Phys B Condens Matter 653:414655–414711

52. Das S, Yang C-Y, Lu C-H (2013) Structural and optical properties of tunable warm-white light-emitting ZrO2:Dy3+-Eu3+ nanocrystals. J Am Ceram Soc 96:1602–1609

53. Santillán-Reyes GG, Pfeiffer H (2011) Analysis of the CO_2 capture in sodium zirconate (Na_2ZrO_3). Effect of the water vapor addition. Int J Greenh Gas Control 5:1624–1629

54. Nakamoto K (2009) Infrared and Raman spectra of inorganic and coordination compounds, part B: applications in coordination, organometallic, and bioinorganic chemistry. John Wiley Sons

55. Mendoza-Nieto JA, Pfeiffer H (2016) Thermogravimetric study of sequential carbonation and decarbonation processes over Na_2ZrO_3 at low temperatures (30–80 °C): relative humidity effect. RSC Adv 6:66579–66588

56. Madhusudhana HC et al (2016) Effect of fuels on conductivity, dielectric and humidity sensing properties of ZrO_2 nanocrystals prepared by low temperature solution combustion method. J Asian Ceram Soc 4:309–318

57. Lara-García HA, Pfeiffer H (2017) High and efficient Li_2CuO_2-CO_2 chemisorption using different partial pressures and enhancement produced by the oxygen addition. Chem Eng J 313:1288–1294

58. Martínez-dlCruz L, Pfeiffer H (2012) Microstructural thermal evolution of the Na_2CO_3 phase produced during a Na_2ZrO_3–CO_2 chemisorption process. J Phys Chem C 116:9675–9680

59. Zhou D et al (2022) The effect of Na_2ZrO_3 synthesis method on the CO_2 sorption kinetics at high temperature. Carbon Capture Sci Technol 3:100050–100058